Biosensors and Bioelectronics 160 (2020) 112218

Contents lists available at ScienceDirect

Biosensors and Bioelectronics

journal homepage: http://www.elsevier.com/locate/bios

Terminal-conjugated non-aggregated constraints of gold nanoparticles on lateral flow strips for mobile phone readouts of enrofloxacin

Run Tian[a,1], Jinyu Ji[b,1], Yangyang Zhou[a], Yumei Du[a], Xiaojun Bian[a], Fulin Zhu[a], Gang Liu[d], Shengyuan Deng[c,*], Ying Wan[b,**], Juan Yan[a,***]

[a] *Laboratory of Quality and Safety Risk Assessment for Aquatic Products on Storage and Preservation (Shanghai), Ministry of Agriculture; Shanghai Engineering Research Center of Aquatic-Product Process & Preservation; College of Food Science and Technology, Shanghai Ocean University, Shanghai, 201306, China*

[b] *School of Mechanical Engineering, Nanjing University of Science and Technology, Nanjing, 210094, PR China*

[c] *Key Laboratory of New Membrane Materials, Ministry of Industry and Information Technology, School of Environmental and Biological Engineering, Nanjing University of Science and Technology, Nanjing, 210094, PR China*

[d] *Division of Chemistry and Ionizing Radiation Measurement Technology, Shanghai Institute of Measurement and Testing Technology, Shanghai, 201203, PR China*

ARTICLE INFO

Keywords:
Lateral flow biosensor
Aptamer
Terminal deoxynucleotidyl transferase
Enrofloxacin
AuNP proximity

ABSTRACT:

Antibiotics abuse now poses a global threat to public health. Monitoring their residual levels as well as metabolites are of great importance, still challenges remain in *in situ* tracing during the circulation. Herein, taking the typical antibacterial Enrofloxacin (ENR) as a subject, a paper-based aptasensor was tailored by manipulating a duo of aptameric moieties to "sandwich" the target in a lateral-flow regime. To visualize the tight-binding sandwich motif more vividly, an irregular yet robust DNA-bridged gold nanoparticles (AuNPs) proximity strategy was developed with recourse to terminal deoxynucleotidyl transferase, of which the nonaggregate constraining feature was unveiled via optical absorption and scanning probe topography. This complex performed exceptionally better in the test strip context than single-particle tags, leading to an enhanced on-chip focusing. Rather than qualitative color developing, further efforts were taken to visualize the readouts in a quantitative manner by exploiting the smartphone camera for pattern recognition along with data processing in a professional App. Overall, this prototyped contraption realized a rapid and ultrasensitive quantification of ENR down to 0.1 μg/L along with a broad linear range over 5 orders of magnitude, plus excellent selectivity and precision even for real samples. Such innovative fusion across DNA-structured nanomanufacturing and intelligent perception provides a prospective and invigorating solution to point-of-care inspection.

1. Introduction

Enrofloxacin (ENR) is a broad-spectrum antibacterial in a major form of quinolone, and its fluoride derivatives also popularizes in veterinary medicine as efficacious antimicrobials (Trouchon and Lefebvre, 2016). However, the abuse of ENR afflicts multiple ill effects upon mankind, including chronic and acute toxicity, allergy, terato-/carcinogenic mutation, and gastrointestinal flora imbalance, *etc.* (Annan-Prah et al., 2012; Janecko et al., 2016; Li et al., 2013). Considering the hazards, many countries have legally restrained the threshold of ENR residues in animal tissues, which vary in the range of 100∼500 μg/kg (Li et al., 2019; Xu et al., 2015). As such, a routine track-down of ENR trace poses a critical act in light of food security and public health. Conventional measures adopt sophisticated instrumentation, including (high performance) liquid chromatography-tandem mass spectrometry and capillary electrophoresis (Denadai and Cass, 2015; Tayeb-Cherif et al., 2016; Terrado-Campos et al., 2017; Tian et al., 2016; Xu et al., 2015). Despite their acknowledged high sensitivity and accuracy, laborious and lengthy sampling and gearing up are necessitated as well, needless to say the complexity in statistics and data interpretation, both of which could not fully meet the situational demands for ENR inspection. To circumvent those issues, several point-of-care testing (POCT) solutions were

* Corresponding author.
** Corresponding author.
*** Corresponding author.
E-mail addresses: sydeng@njust.edu.cn (S. Deng), wanying@njust.edu.cn (Y. Wan), j-yan@shou.edu.cn (J. Yan).

[1] These authors contributed equally to this work.

https://doi.org/10.1016/j.bios.2020.112218
Received 14 February 2020; Received in revised form 7 April 2020; Accepted 14 April 2020
Available online 18 April 2020

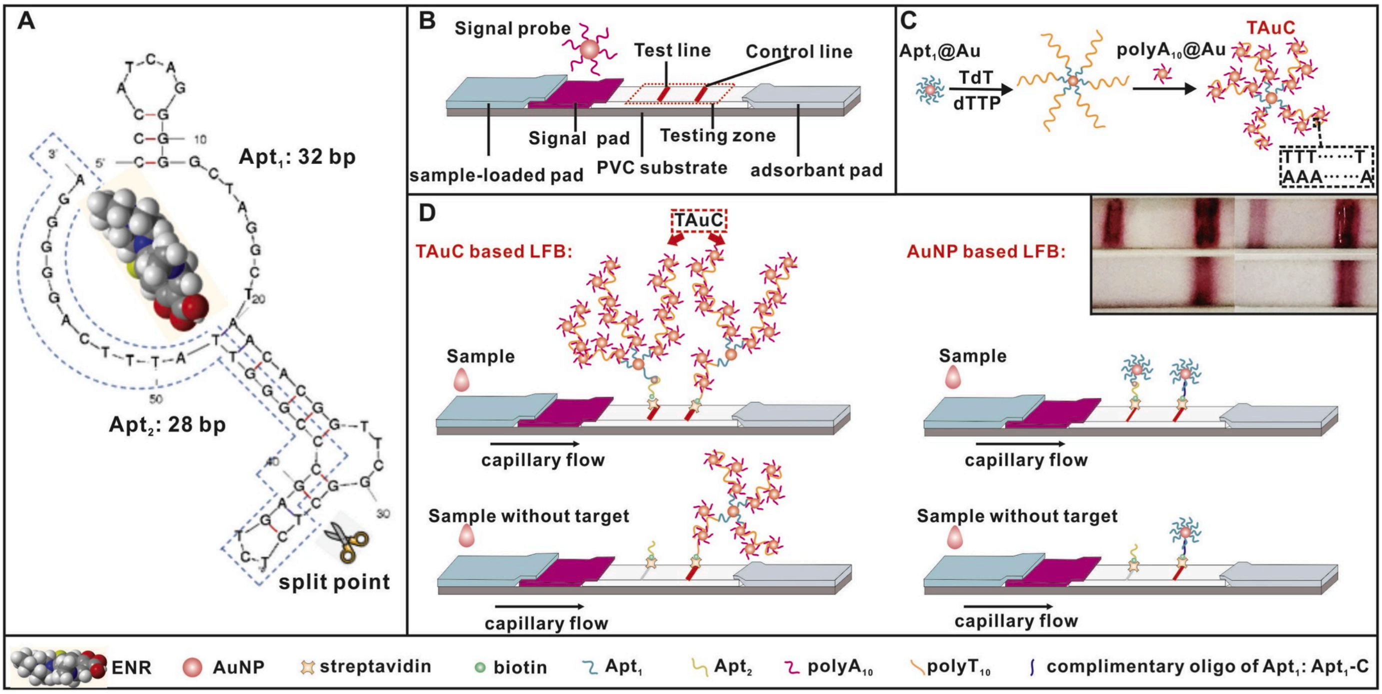

Scheme 1. **(A)** The aptamer motif and the assignment of Apt_1 and Apt_2. **(B)** Anatomy of a lateral flow ENR sensor, revealing key components. **(C)** The catalytic assembly of $polyA_{10}$@ Au on the branches of Apt_1@Au. **(D)** Schematic illustration about the working principles of TAuC (left) and AuNP (right)-visualized LFB with (upper) and without (lower) the target. **Inset:** The corresponding snapshots to the four combinations on the chromogenic prototypes.

proposed and implemented properly in the regimes of enzyme-linked immunosorbent assay (ELISA), colorimetry, and above all else the test strips (Hu et al., 2019; Kim et al., 2015; Li et al., 2019; Majdinasab et al., 2019).

Dated back to the born of the diabetes dipstick in 1950s (Free et al., 1957), the lateral flow-based biosensor (LFB) has made significant development so far, which now could handle field speciation analyses out of a realistic matrix quite handily and efficiently (Chen et al., 2016b; Choi et al., 2017; Fu et al., 2016; Lee et al., 2019; Lin et al., 2018; Quesada-González and Merkoçi, 2015; Quesada-Gonzalez et al., 2019). A key constituent in their builds lays at the recognition module, which normally runs on the immunoaffinity (Preechakasedkit et al., 2018; Qi et al., 2019). Though inherently specific, the antibodies could hardly stand dehydrated adsorption and long-term storage in such miniaturized devices; while pairing with tiny immunogenic targets turns into another downside. To fill in these technical breaches, artificial aptamers rise to those uncharted POCT contexts in clinical diagnosis and checkpoint screening by virtues of their programmable epitopes, flexible motifs plus a short-cycle expression (Bostan et al., 2017; Chen and Yang, 2015; Dalirirad and Steckl, 2018; Jauset-Rubio et al., 2016). For typical examples, a lateral flow aptasensor adapted the competitive assay for the detection of picomolar β-conglutin with gold nanoparticle (AuNP) as the transducer (Jauset-Rubio et al., 2016). Taking privileges of the sandwich format, an aptameric twin collaborated the Vaspin binding successfully, one of which was biotinylated as capturer while the other also conjugated with AuNPs for signaling relay (Ahmad Raston et al., 2017). Later on, inspired by the recombinant single-chain variable fragment (ScFv), site-specific aptamer cleavage sprang up as a competent alternative to the previous cognate matching scheme (Chen et al., 2016a). On the other hand, current LFBs on sale relied solely on single-particle labeling with no exceptions (Quesada-Gonzáleza et al., 2019). Unfortunately, though falling in a wider UV–Vis spectrum, the AuNP aggregation-induced colorimetry could be disrupted and degraded so easily in natural fluids that was ineligible for field practices (Kang et al., 2010). Therefore, in pursuit of a more discriminable transduction, it is desirable to introduce some robust and cost-effective amplifier that would match the solid-state LFB environment (Bishop et al., 2019; Fu et al., 2019; He et al., 2018; Kasetsirikul et al., 2020; Wang et al. 2017, 2018).

Herein, to adapt the joint merits of LFB and molecular probes for ENR monitoring, a novel doublet of ENR aptamers, namely Apt_1 and Apt_2, were synthesized for strategic tailoring. The thiolated Apt_1 (SH-Apt_1) was tagged with AuNP into Apt_1@Au adduct, whereas the biotin-modified Apt_2 (bio-Apt_2) loaded on the test area via streptavidin coupling. In the presence of ENR, the dual fragments pinched it up as a whole. To enhance the readouts, a so-called end-regulated AuNP clustering (TAuC) method was developed with recourse to the terminal deoxynucleotidyl transferase (TdT)-directed polymerization (Fowler and Suo, 2006). The enzyme extended the frayed 3'−OH of Apt_1 to a polythymine (polyT_n) chain, which thereby hybridized with spherical nucleic acids (A_{10}@Au), resulting in a massive proximity of AuNPs with highly coherence and resilience to influences from solvation and capillary as well. Such drastic change in surface chemistry led to a substantial hyperchromicity as the ensemble migrating forward and focusing onto a stripe. This dynamic chromatism on chip further received an intelligent perception that was visually quantified through a smartphone camera in a home-developed application (App). Overall, the compact prototype with the built-in neat protocol achieve a swift, accurate and ultrasensitive analysis of ENR over a broad window, which would complements the defects of common LFB in semi-quantitative and lackluster responsive.

2. Experimental

2.1. Materials and reagents

All synthetic DNA primers were ordered from Sangon Biotech with sequences tabulated in Table S1 (Du et al., 2019; Liu et al., 2017). Agarose (0.8 wt%), phosphate buffered saline (PBS, 20x, pH 7.4), 250 base-pair ladder Marker, deoxyadenosine triphosphate (*d*ATP, 100 mM), tris(hydroxymethyl)aminomethane/acetic acid/ethylenediamine tetra-acetic acid (EDTA) (TAE, 50x, pH 8.4), streptavidin and Enrofloxacin

(ENR) were also procured from Sangon. Terminal deoxynucleotidyl transferase (TdT, 5 U/μL) was purchased from Beyotime Biotechnology. All solutions were prepared with Milli-Q ultrapure water.

2.2. Modification of AuNPs with DNA strands

AuNPs were prepared with the reported salt aging approach (Grabar et al., 1995; Hurst et al., 2006). In this study, two kinds of DNA-capped Au were assembled: Apt_1@Au and $ployA_{10}$@Au. Briefly, 20 μL of DNA in interest, *e.g.* SH-Apt_1 was mixed with 1 mL of as-prepared AuNPs and incubated at 25 °C overnight, followed by the addition of 113 μL of 0.1 M PBS. After 30-min vortex, the conjugates were aged in 10 mM pH 7.0 PBS containing 2 M NaCl to reach a final concentration of 0.15 M and stood still. After the removal of excessive reagents by 15-min centrifugation at 12,000 rpm, the precipitates were re-dispersed and centrifuged again for 3∼4 rounds. The extracted Apt_1@Au was suspended in 200 μL of deionized water and stored at 4 °C for later use.

2.3. Association of biotinylated DNA with streptavidin

5 μL of 1 mg/mL streptavidin in 10 mM pH 7.4 PBS was blended with 35 μL of 5 μM bio- Apt_2 solution and incubated at 4 °C for 2 h. The mixture was ultra-filtrated at 6000 rpm for 30 min to remove superfluous Apt_2. After washing twice with PBS, the couple of streptavidin-(bio-Apt_2) was dissolved in PBS and kept at 4 °C. Likewise, the streptavidin-(bio-$polyA_{10}$) was conjunct in the same process.

2.4. Terminal catalysis-driven AuNP attraction

50 μL of the as-received TdT was pipetted into 200 μL of Apt_1@Au in stock to catalyze the epitaxial grafting of Apt_1 at the coexistence of adequate deoxythymidine triphosphate (*d*TTP). Once upon 1-h elongation, the reaction was halted by denaturing at 70 °C for 3 min. The produced dendrimer ($polyT_n$-Apt_1@Au) was subsequently crosslinked with its complementary counterpart $polyA_{10}$@Au, conglomerating to TAuC as previously denoted.

2.5. Fabrication of lateral flow sensing device

A LFB in one piece was composed of five parts (Scheme 1A): the Substrate, the Detection Pad, the Sample Pad, the Signal Pad, and the Absorption Pad. First, a polyvinyl chloride (PVC) sheet with the geometry of 5 mm × 62 mm was stretched flat as the capillary bed. Next, a pristine glass fiber foil in rectangular shape (5 mm × 12 mm) was trimmed off as a droplet-docking bay, whereas its gilded variant was specified for reporter attachment by submersing in the aqueous AuNPs then oven-dried at 80 °C for 30 min. Thirdly, two domains formed up the test area that was pretreated with 2 mg mL^{-1} streptavidin for 30 min: one further covered with bio-Apt_2 (*i.e.* Test Line) and the other reserved for bio-$polyT_{10}$ (Control Line). Both desiccated in the open air at ambient temperature for 1 h. To end up, the foregoing divisions were tiled up in orders along the PVC bottom, and tailgated by 2-mm overlap to secure the specimen permeation and seamless channeling throughout the strip, which lied just as it was in a cassette ready for future disposal.

2.6. Smartphone-based one-stop enrofloxacin assay

The aliquoted Enrofloxacin dilutions in PBS were administered onto the Sample Pad. After 5-min wicking, the test subjects were pictured in batches in the scope of the main camera (dual lenses; 48 megapixels; f/1.8 wide aperture, 1/2.0″ max magnification, equivalent focal length: 0.8 μm, Phase Detection Auto Focus technology) of a Huawei Honor View 20 smart-phone from a self-made stand under normal laboratory lighting. A mobile App was home-developed with the integrated software development kit (SDK) Android Studio 3.5.3, debugged and ran in Android 9.0 operating system (OS).

The App accessed to the camera automatically to recognize Test Line (T.L.) and Control Line (C.L.) by addressing them in a pair of green sampling frames in display. It counted pixels in these sectors by converting RGB scheme to decimal grayscale ($g = 0.333 \cdot (R + G + B)$). To correlate the color gradient with the ENR amount, c_{ENR}, we defined a new metric as the normalization of gray values (I), *i.e.* the fraction of $I_{T.L.}$ versus $I_{C.L.}$ (or simply T.L./C.L. as demonstrated in Fig. 3B), in which $I_{T.L.}$ and $I_{C.L}$ came from the subtraction of $(255 - g_{T.L.})$ and $(255 - g_{C.L.})$, respectively.

All experiments were repeated for at least three times in parallel. Other typical antibiotics, such as Ciprofloxacin (CIP), Norfloxacin (NOX), Lincomycin (LIN), Chloramphenicol (CHL), Streptomycin (STR), Ofloxacin (OFX), and Kanamycin (KAN) were picked up as homologous interferents to interrogate the selectivity.

2.7. Real sample analysis

To emulate field exercises, three processed foods in the domestic Family Mart were chosen, including skimmed milk powder, surimi homogenate, and honey drops. Different concentrations of ENR (0.1, 1, 10 and 100 μg/L) were spiked into these products and mixed for further detection. 10 μL of each sample solution were examined by LFB in a row in terms of the recovery.

3. Results and discussion

3.1. Proof-of-concept study on lateral flow biosensing

Scheme 1 illustrates the workflow of a model LFB, that comprises five basic modules as designated in Scheme 1B. On such mini platform, the ENR analysis started with liquid dispensing at the left-end inlet. According to Young-Laplace equation (Atencia and Beebe, 2005), capillary action rules inside the natural microfluidic channels across the fibrous film that pumps the flow towards the outlet on the right (Li et al., 2012). Different from the pregnancy test stick where AuNPs responses individually to single hCG (human chorionic gonadotropin) hormone in a strict 1:1 stoichiometry (Gnoth and Johnson, 2014), herein a colorimetric multiplication was designed as an updated version to the previous probing method. In details, an intact ENR-selective aptamer got cleaved into two haptens (Scheme 1A) - Apt_1 and Apt_2 (Du et al., 2019). On one hand, a great deal of Apt_1 anchored densely upon AuNP surface via the ordinary Au−(5′-thiol) binding. On the other side, the exposed 3′-hydroxyls strung those freestanding *d*TTP successively under enzymatic catalysis of TdT. This template-free growth proceeded fiercely that radiated the Apt_1@Au core into a highly divergent morphology like a sea urchin. Its outreaching polymeric arms ($polyT_n$) hand-shook openly, simultaneously and tightly with several $polyA_{10}$@Au partners (Scheme 1C). Furthermore, the two building blocks cooperated, cascading such dendritic landscape into a golden network in spontaneity. This unusual condensed state drew a mass of AuNPs in so close vicinity that could replace the mere AuNPs on chip for an online colorimetric amplification.

In continue, the second stage began as ENR arrived at the TAuC reservoir (Scheme 1D). Though the atmospheric pressure could somehow prevent the water loss in debt to the porous texture of the membrane, hence encompassing a shallowly hydrated micro-environment, the introduction of analytes would deeply wet this region to mobilize the dwelling species. During the infiltration, ENR molecules bumped into TAuC entities that were floating away. In general, there were two possible entries for ENR to Apt_1: either bound directly with the non-extended Apt_1 (Liu et al., 2017), or substituted $polyA_{10}$@Au. Presumably from the Einstein-Stockes formula (Wu et al., 2010), the complex as a bulky whole should diffuse slowly but collectively on its way through the aqueduct towards the upcoming check station. The second half of the aptamer bio-Apt_2 had been immobilized at this stop on a thin coating of streptavidin beforehand, and it synergized with Apt_1 altogether to pin ENR down to the base. At this point, a sandwich-typed DNA-skeletal

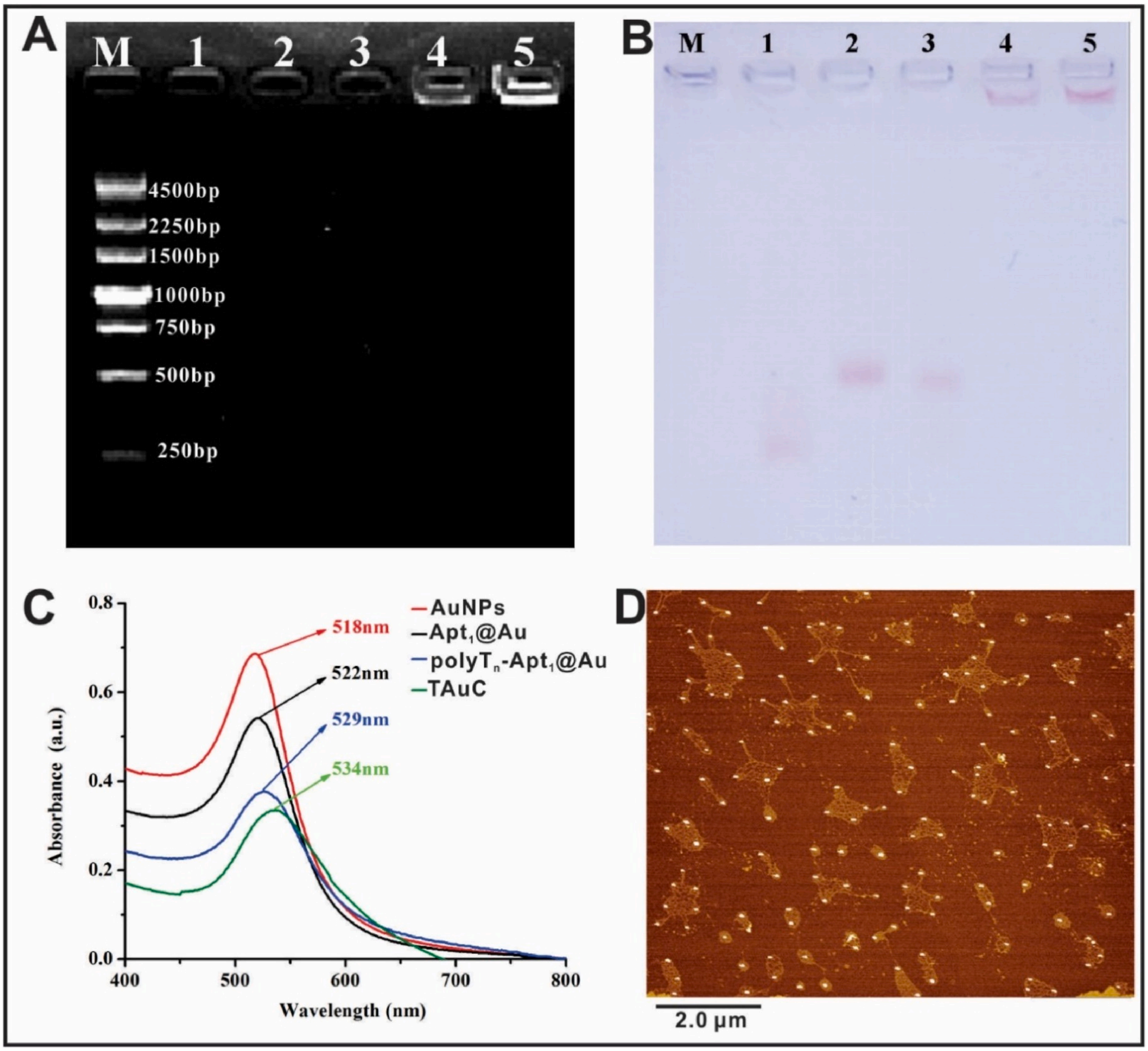

Fig. 1. Gel exposure out of the agarose electrophoresis under **(A)** UV lamp and **(B)** white light. Lanes from left to right: marker **(M)**, polyA$_{10}$@Au **(1)**, Apt$_1$@Au **(2)**, mixture of polyA$_{10}$@Au and Apt$_1$@Au **(3)**, polyT$_n$-Apt$_1$@Au **(4)**, and TAuC **(5)**. **(C)** UV–Vis absorption spectra of AuNPs **(red)**, Apt$_1$@Au **(black)**, polyT$_n$-Apt$_1$@Au **(blue)**, and TAuC **(green)**. **(D)** A microscopic magnification of TAuC tapped by AFM. Scale bar:2 μm. (For interpretation of the references to color in this figure legend, the reader is referred to the Web version of this article.)

structure emerged *in situ* that erected tall within the narrow band. Consequently, the originally fair distribution of TAuC now concentrated over this space whilst mounting atop Apt$_1$. As a result of this crowding effect, a red ribbon stood out to the naked eye. Meanwhile, those unreacted TAuC overdose was eluted farther and recycled at the reference spot by polyA$_{10}$, where the red belt always visible. In this case, there shall be two straps in sight as shown in Scheme 1D inset, thus enabling a ratio-metric readout. Otherwise, the absence of ENR would bring about a null-indicating situation in which only the Control Line turns red. Whichsoever, the color out of TAuCs looks much brighter than those from the sparsely scattered AuNPs as depicted in the right column of Scheme 1D also in the corresponding inset. As a preliminary, even for an intermediate 100 μg/mL ENR, this kind of traditional LFB just presented a reddish appearance at most, which demonstrates the superior resolution of TAuC-based LFB in visual identification of tracing ENR.

3.2. Characterization of terminus-regulated AuNP clusters

To verify the formation of TAuC, its optical and structural properties were characterized. First things first, agarose gel electrophoresis was recruited to evaluate the content of DNA in various Au/DNA configurations, which were subjected to post stain with ethidium bromide and then ultraviolet irradiation in a transilluminator. As aligned in the consecutive wells of Fig. 1A, neither polyA$_{10}$@Au (Lane 1) nor Apt$_1$@Au (Lane 2) manifests the sign of electrophoretic motility, suggesting apparently that the dimension of the two fall behind that of even the tiniest marker in Lane M. Noteworthily, although both polyA$_{10}$ and Apt$_1$ appear linear on their own conformation, their gold ensembles converged multistrands into a compact composite, that bore resemblance with the coiled/circular RNA; in the meantime, its zeta-potential shifted negatively as compared with that of the salt-stabilized AuNPs as well as the solvated pure nucleotide chains. In this sense, these two aspects were supposed to contribute to the boosted movement of DNA@Au under applied voltage. Nevertheless, due to the volume exclusion of AuNP, the total capacity of DNA became too diluted to account for an appreciable retention. In view of this, we switched to brightfield as an alternative condition of observation, and it turns out to be an obscure pinkish patch at a distance in line with 250 bp as can be seen in Lane 1 of Fig. 1B, which fades out with a faint trail of larger molecular weights. The color derives directly from AuNP itself, not the groove-intercalating pigment. In this way, the density of polyA$_{10}$ (equivalent to 5 bp) on AuNP was inferred to be 50 (~250/5) on

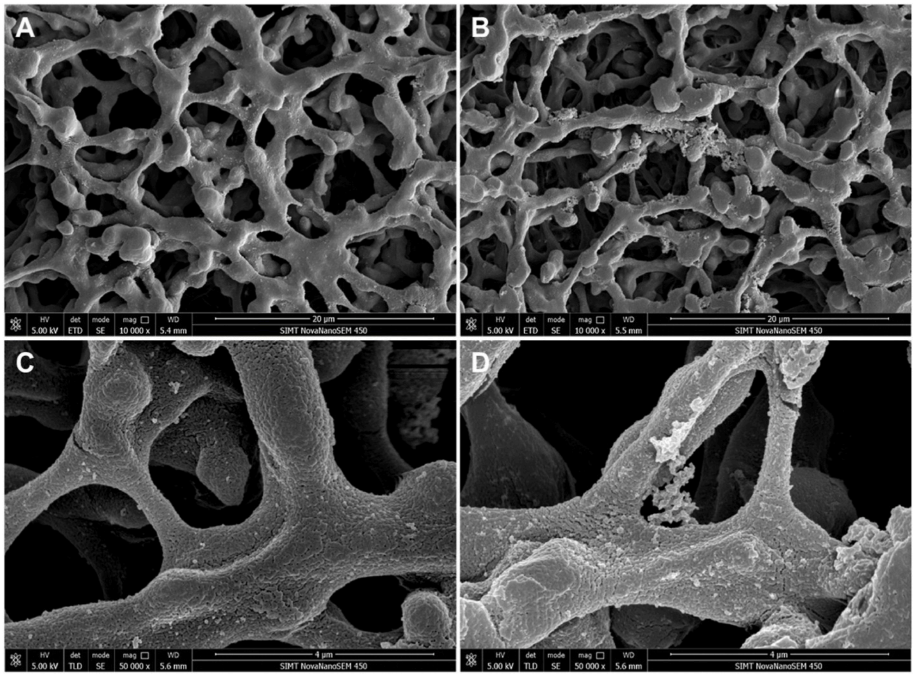

Fig. 2. SEM images of glassy fiber at a LFB test line without **(A)** and with (B) the introduction of ENR. Scale bar: 20 μm. (C) and (D) are the corresponding local magnification at a scale bar of 4 μm.

average. More obviously, the directional motion of Apt_1@Au was spotted in Lane 2 that ends around 500 bp, which means the coverage (ligancy) of the longer Apt_1 (~20 bp) halved to 25 per AuNP due to its relatively greater steric hindrance. This pattern complies with the general rule that the mobility is inversely proportional to the logarithmic base pairs (Southern, 1979). Therefore, regardless of the full-length emptiness in the darkfield, Apt_1@Au was in fact nicely separated from polyA_{10}@Au in their mixture by taking advantage of the intrinsic sieving effect in solidified gel (Zanchet et al., 2002) as witnessed in Lane 3, which also proved no entanglement there was between Apt_1 and polyA_{10}. Unexpectedly, the product out of the catalytic addition (poly-T_n-Apt_1@Au) stuck in the entry port of Lane 4, in stark contrast to those pitch-black lanes in Fig. 1A, which highlights the savage sprawl of polymeric overhangs during the fast turnover of TdT (Wan et al., 2015). Based upon a rough calculation, a dramatic extension would be obtained far beyond 160 bp ($n > (4500-500)/25$) within 1-h reaction. Of note, there are not any low traces below 4500 bp, implying a fully isotropic sprout from all the Apt_1@Au seeds. Now the total capacity on a singular AuNP had surged by eight folds, seemingly close to that of a plasmid (Ding et al., 2014). Ideally, over 16 copies of polyA_{10}@Au could be stacked in a tail-to-head fashion alongside the polyT_n. This leads to a darker red in the slot of Lane 5, which seems consistent with the deepening in Fig. 1A. Also, one cannot catch sight of the same imprint of polyA_{10}@Au downstream as in Lane 1, a convincing proof that they had been made full use. Together in a nutshell, these phoretic phenomena confirm the organization of a super-structured polyA_{10}@Au-polyT_n-Apt_1@Au, *i.e.* the dubbed TAuC.

In the second place, UV–Vis spectroscopy was employed to take an insight of peripheral changes on the surface states of AuNPs. The initial AuNPs with citrate as the capping agent has a pronounced absorption at 518 nm (Fig. 1C, red curve), which is ascribed to the inherent surface plasmon resonance (SPR) of metallic nanocrystals (Amendola et al., 2017). Dividing its absorbance (A_{SPR}) by that at 450 nm (A_{450}) enables an evaluation on the diameter (d) of AuNP to be ~14 nm with reference to Haiss's empirical fit [$d = \exp(3 \cdot A_{SPR}/A_{450} - 2.2)$] (Belmouaddine et al., 2018). The surficial substitution with Apt_1 (Apt_1@Au) red-shifted the peak to 522 nm (black curve), yet both the FWHM (full-width at half maximum) and the fraction of A_{SPR}/A_{450} (≈1.75) retained mostly, indicative of a well-preserved size even after the ligand exchange (Kim and Lee, 2009). In comparison, the profile of polyT_n-Apt_1@Au displays a bathochromic move to 529 nm of the extremum (λ_{SPR}, blue curve). More than that, the FWHM expands, signifying a wider size distribution owing to the fluctuation in polymerization degree. Nonetheless, the normalized local SPR attenuated to 1.56, that essentially reflects an interfacial rearrangement caused by the repellence among over-expressed T-spines, and accordingly, a subtle crystalline reshape. Counting in this complication, a tantamount expression related to wavelength was adopted to rectify $d = \{\ln[(\lambda_{SPR} - 512)]/6.53\}/0.0216 \approx 44$ nm (Amendola et al., 2017). Last but not the least, with respect to TAuC ($\lambda_{SPR} = 534$ nm, green curve), both formulae reached a consensus on $d \approx 56$ nm. Concomitantly, an even broader absorption came up, which could virtually be deconvoluted to one peak belonging to polyA_{10}@Au and the other to Apt_1@Au. A simple superposition also makes sense of this judgement that d[polyA_{10}@Au] plus d[polyT_n-Apt_1@Au] approximates the nominal d[TAuC], assuming polyA_{10}@Au shares a very close radius with Apt_1@Au and bare AuNP. On this account, this behavior should not be accredited to the well-known hybridization-mediated aggregation of AuNPs (Sato et al., 2003). Because if so, there must have been a conspicuous color variation from magenta to violet as a consequence of scattering properties (Zhou et al., 2015). The Lane 4 and 5 of Fig. 1B in an indistinguishable wine red also supports this inference. Moreover, provided the molar extinction coefficient (the absorptivity, $\varepsilon_{450} = 1.76 \times 10^8$ M^{-1} cm^{-1} for polyA_{10}@Au, polyT_n-Apt_1@Au: 6.65×10^9, and TAuC: 1.41×10^{10}), the rations of AuNP with the two disparate polymer shells are possible to figure out by the Beer−Lambert's Law (Ung et al., 2002). Hence, through spectral analysis in a mind of linear combination, a unique DNA-bridged multi-gold construct, *i.e.* TAuC, came into being, which shall give credit to TdT.

On the third move, direct microimaging was taken to corroborate the last claim about the construction of TAuC. As topo-graphed in the tapping-mode atomic force microscope (AFM) (Fig. 1D), the TAuC drop-casts turn out to be a "thousand islets" scenery upon a sliced piece of mica plate. In such a geothermal-liked map, a handful of white dots at higher altitudes grasp the eye, which ought to be recognized as polyT_n-Apt_1@Au ($d \approx 44$ nm) in minority. The reason for that is perceived as they are surrounded by indiscernible yet far more populated particulate

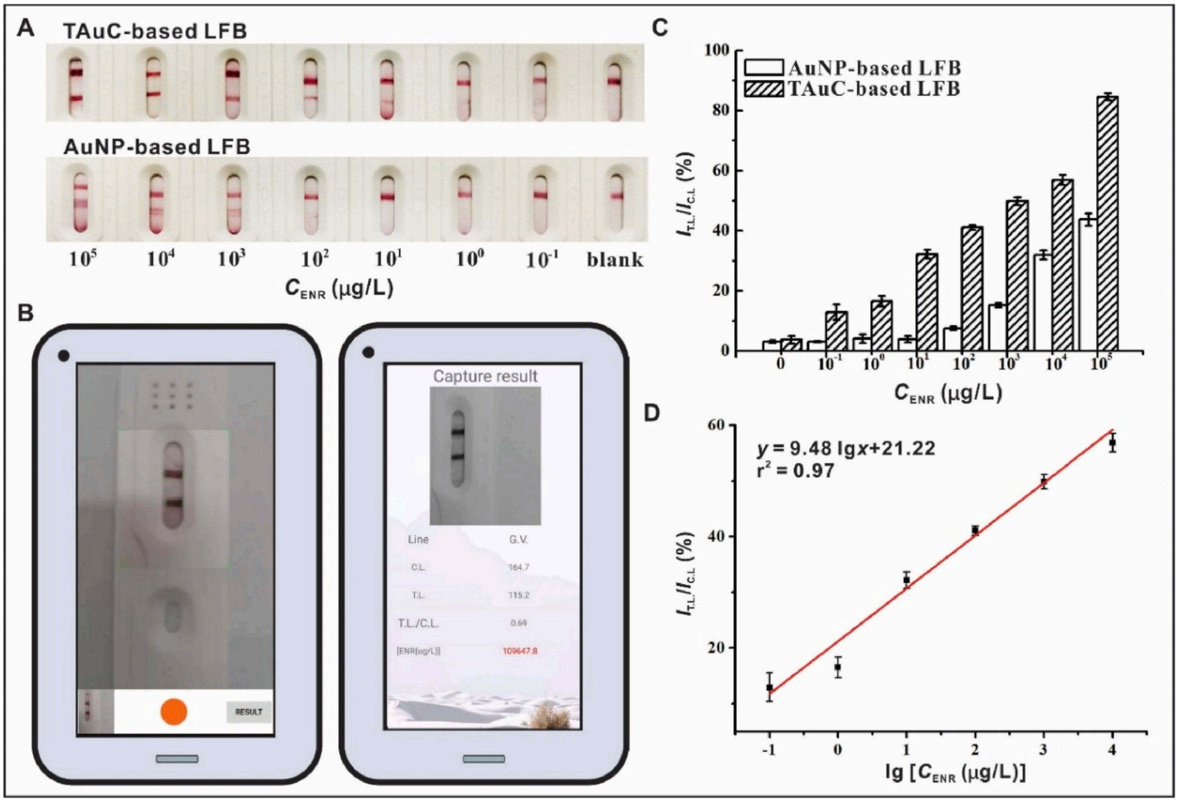

Fig. 3. **(A)** Representative LFB palettes based upon TAuC **(upper)** and AuNP **(lower)** in a sequence from high **(left)** c_{ENR} to low until blank **(right)**. **(B)** Screenshots of a molded LFB in position **(left)** and the App UI under development **(right)**, which is adaptable to any Android 9.0 mobile termini. **(C)** Histograms about the gauged gray value (I) as a function of logarithmic c_{ENR} for the AuNP **(unfilled)** and the TAuC **(hatched)**-dictated LFB, respectively. **(D)** The corresponding calibration curve of the TAuC-governed LFB.

matters, that by zoom in cannot be anything but polyA$_{10}$@Au ($d \approx 14$ nm). As such, this two-dimensional top-view sheds light on the anatomy of TAuC. Interestingly, although a majority of particles stay too close to resolve themselves in single, each one still maintained its physical boundary independently against collapse to giant agglomerates, which justifies the relationship among the absorptive plots in Fig. 1C. Some golden patches even expand over a large scale of 2 × 2 μm^2, that is believed to take place by the successive feeds of polyA$_{10}$@Au the satellite along TdT-prolonged polyT$_n$-Apt$_1$@Au the backbone. The latter are largely compartmentalized in a few and circumscribed by well-defined borders. Notably, from isolated Apt$_1$@Au to their colony nearby, serpentine passages stretch out like axons so long as ~1 μm. As a matter of fact, this layout unveils the anisotropic characteristics about how DNA propagated catalytically. And kinetically, the adjacent polyT$_n$ entangled by chance to draft a basic fabric of the foundation at the beginning **(1)**, onto which polyA$_{10}$ preferred to anchoring; in return, they created more rendezvous or transition sites between Apt$_1$@Au **(2)**; and ultimately, AuNPs filled up the inner space and packed closely into a gold-studded textile **(3)**. Among the three phases, step **(1)** plays a decisive role for both the ductility and the tacticity of polyT$_n$ were "terminus-regulated" (Deng et al., 2019). In theory, the density/roughness of polyA$_{10}$@Au can be estimated by localized line-scans, which does favor to sensitize the ENR response in a cascade of n AuNPs *vs.* 1 target rather than the old chemometrics in 1 AuNP *vs.* 1 target (Zhao et al., 2008). Concurrently, the Au neighborhood as a sub-microscale unity could swim freely in the porous matrix of the Multimode fiber (Φ: ~120 μm); whilst its compactness held a good hydrodynamic stability. Besides, the DNA web full of negative charges facilitated a diffusiophoresis against the silanol-carpeted glassy walls (Che et al., 2015). In addition, such level of surface potential is able to withstand electrostatic and rheologic co-precipitation in TAuC dispersion, which prevails over the *meta*-stable AuNP aggregates susceptible to salts (Zhang et al., 2013). All in all, the above-mentioned characterization validated the facile partition of TAuC that features comprehensive quality suitable for the LFB scenarios.

3.3. TAuC-sensitized lateral flow assay on enrofloxacin

The identified TAuC was delivered to LFB and deployed throughout the Signal Pad prior to the ENR quantification. Once zooming in by a scanning electron microscope (SEM, JEOL JSM-6700F), we could take a glance at the local porosity of the T.L. (Fig. 2). Over the microregion without the targets (Fig. 2A), the local fiber bundles were dotted with streptavidin-bio-Apt$_2$ conjugates (Fig. 2C). On the other hand, the glassy surface became rougher and less clean in the presence of ENR (Fig. 2B), where some tufted adsorbents came to our eyes. These xenografts embedded in the central Fig. 2D could be no other than TAuC. The whole composition not only suggests the scale of the aptameric complex in a riddled foreground, but also inspired how TAuC permeated and tunneled through the film so accessibly.

In a comparative style, the analyte with a variety of concentrations (c_{ENR}) from 0.1 to 10^5 μg/L were syringed onto two LFB arrays as horizontally merged in Fig. 3A. Abiding by the established parameters in our previous paper (Du et al., 2019), the optimal running buffer was 0.1 M pH 7.4 PBS containing 0.15 M NaCl. Ensuing a flash incubation in 5 min at room temperature, either one or two red bands developed on the white baseboard, testifying this LFB gizmo functions as expected. At all events, the Control Line (C.L.) that sits at a higher place rendered red strongly. On the contrary, the color faded in at the Test Line (T.L.) below as c_{ENR} escalates. For TAuC-entrapped LFB (upper panel), it would be slightly difficult for the human eyesight to observe the weak coloration at 0.1 μg/L on the right next to the blank. Pertaining to the regular AuNP

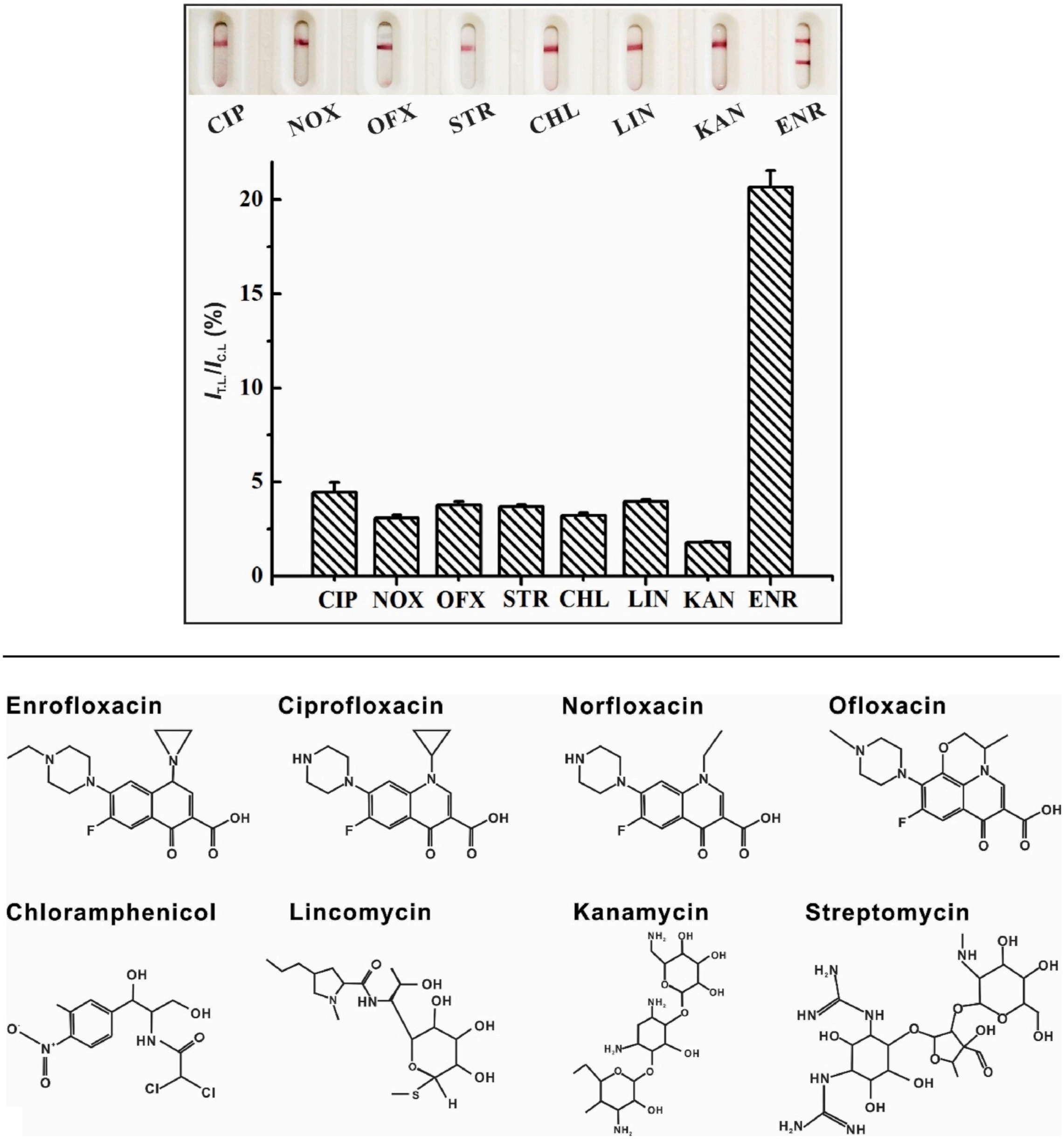

Fig. 4. Upper panel: A compilation of the resultant App readings. **Inset:** A panorama of interference tests on the TAuC-based LFB. **Lower panel:** Molecular structures of ENR and interfering species including Ciprofloxacin (CIP), Norfloxacin (NOX), Ofloxacin (OFX), Chloramphenicol (CHL), Lincomycin (LIN), Kanamycin (KAN), and Streptomycin (STR).

(lower panel), the vision limit lifted to 100 μg/L on the fourth from left. In a vertical perspective, one would notice that the T.L. of each TAuC system behaves more remarkable than that of AuNP at equimolar ENR, which underscores the primary superiority of TAuC over AuNP in probing ENR residual especially at ultralow c_{ENR} in a minute dispense of 10 μL. In other words, melding with synthetic polyT$_n$ did not disrupt the allostery of the fragmented Apt$_1$ (Chen et al., 2016a), which let out no sign of affinity loss. The secondary benefit from labeling with TAuC would be the negligible incidence of backflow from Signal to Sample Pad (Koczula and Gallotta, 2016), because of its smaller diffusivity and weaker wettability (solubility) than AuNP. Evidently, the alignment of all three demos on the left have AuNP stick to the upstream underutilized, which definitely impacts the ratiometric precision. Conversely, none waste of TAuC happened except for the LFB to the 4th from the right, which might arise from a machining fault. Aside from the aforementioned edges, the collection of TAuCs on both T.L. and C.L. barely discolored in the open air (at least for days) or leaked out in the water (data not shown), being much more durable in strong ionic strength (up to 0.2 M NaCl) and tolerant of environmental factors than those photo (chemical)- bleachable phosphors and chemo/pH-responsive agents (Xie et al., 2014).

Distinct from the aggregation-induced absorption in a cuvette or vial (Wang et al., 2016), the indicator of which generates a vivid tone (red, blue, purple), the invention here works in a monochromic mode just like other accessible LFBs on market. This gradation in red suffers from the visual insensitivity - an inconvenience somewhat similar to the dye phenolphthalein in pH titration, that reduces the LFB tool to qualitative practices. In response to this problem, we resorted to the miscellaneous smartphone to improve the result interpretation. As showcased in Fig. 3B left, one LFB in the upper row of Fig. 3A was put flatwise on the bench and exposed below the ceiling lamp (flashlight off) in the central viewfinder of the phone camera, which was fixed perpendicularly in the focal distance away. The photographing was called up by a specialized App, which accomplished an addressable Line recognition followed by

Table 1
Performance appraisals among ENR analytical techniques.

Method	LOD	Recovery	In Situ?	Time	Reference
GC	1 mg/Kg	>78%	No	N/A	Blasco et al. (2009)
Chemical Analysis	0.3 mg/L	88~109%	No	N/A	Xu et al. (2018)
ELISA	0.7 μg/L	75~ 86%	No	N/A	Kim et al. (2015)
HPLC	8 μg/Kg	82~110%	No	N/A	Denadai and Cass (2015)
HPCE	0.17 μg/Kg	N/A	No	N/A	Lombardo-Agui et al. (2010)
TLC	10 mg/Kg	N/A	Yes	N/A	Billah et al. (2014)
LC	0.05 mg/Kg	89~105%	No	N/A	Terrado-Campos et al. (2017)
TdT-RCA	2.5 ng/L	87.5~92.1%.	No	2.5 h	Du et al. (2019)
LFB	0.1 μg/L	90~124%	Yes	5 min	This Work

an instantaneous color transcoding from 24-bit hexadecimal RGB (red/green/blue) to 8-bit binary greyscale (I). Afterwards, the computed pixel integrals of the predefined $I_{T.L.}$, $I_{C.L.}$, and $I_{T.L.}/I_{C.L}$ were tabulated in the user interface (UI) as a screen capture in Fig. 3B right (Please refer to Table S2 for full data set). Conforming to this standard operation procedure (SOP), we set out to digitize the patterned hues one-by-one in Fig. 3A, and compiled in two groups of histograms in Fig. 3C by associating c_{ENR} with $I_{T.L.}/I_{C.L.}$ The ratiometry agrees well with the trends in Fig. 3A, and the TAuC-embedded LFB (the hatched) responds to ENR more intensively and sensibly than AuNP (the unfilled). What is more, their background noises at zero ENR are nearly equal. That is to say, the exploitation of TAuC in LFB undoubtedly promoted its signal-to-noise ratio. A calibration curve was mapped out in Fig. 3D that $I_{T.L.}/I_{C.L}$ (y) $= 9.48 \cdot \lg(C_{ENR}(x)) + 21.22$ (the regression coefficient: $R^2 = 0.97$) from 0.1 to 10^4 μg/L, spanning over 5 orders of magnitudes. The limit of detection was found to be 0.1 μg/L experimentally, being 1000-fold lower than that of the AuNP-dependent LFB. Apart from that, the little error bar on each column testifies the satisfactory reproducibility between five paralleled runs. In short, this brand-new benchmark test succeeded in a real-time quantification of ENR by hyphenating the strengths of TAuC in LFB setup with intelligent assistants, which fulfilled a global outperformance to the end.

To inspect the specificity of this sensing apparatus, bactericidal family members in current over-the-counter (OTC) drugs were double-checked as interferents to ENR at 1 μg/L, including CIP, NOX, OFX, STR, CHL, LIN, and KAN. Both the sensorgrams for survey and their statistic percentages were summarized in Fig. 4, in which the LFB replies positively to ENR only on account of "two strokes" on LFB and a $I_{T.L.}/I_{C.L}$ of ~20%, whereas negatively to the remaining by "one stroke" and their insignificant $I_{T.L.}/I_{C.L}$ (<5%). In essence, it is the judicious epitopic mapping of ENR (1-cyclopropyl-4-oxo-6-fluoro-7-(4-ethylpiperazin-1-yl)-dihydro- quinoline-3-carboxylic acid, in IUPAC nomenclature) that decides the teamwork: Apt_1 flanked the carboxyl moiety while Apt_2 the 4-ethylpiperazin-1-yl (Boughougal et al., 2018). Such partnership between this duo of split aptamers set up an entity of double locks, endowing this sandwiched recognize means with extraordinary selectivity. By the same token, this paradigm would also be qualified to determine multiplexed antibacterials in the lower panel of Fig. 4.

3.4. *Real sample assessments on devised lateral flow strip*

As mocking tests, skimmed milk powder, surimi homogenate, and honey drops were diluted and spiked with ENR aliquots to challenge the plausible practicability of the LFB on trial. From the recovery rates (R) in Table S3 that fluctuate at a decent interval of [90%, 124%], the potential utility of this gadget could be substantiated. The LFB assay was thus established for real at $c_{ENR} \geq 1$ μg/L ($R \geq 90\%$); on the opposite, being not applicable (N/A) for $c_{ENR} < 1$ μg/L.

To exemplify the competency of LFB in ENR sensing, a crosswise comparison was carried out among all sorts of available technologies in Table 1, for instance, Gas Chromatography (GC), Enzyme-Linked Immunosorbent Assay (ELISA), Liquid Chromatography (LC), Thin Layer Chromatography (TLC), High-Performance Liquid Chromatography (HPLC) and Capillary Electrophoresis (HPCE), *etc*.. The LFB serves predominantly as an expedient measure over the others in *in situ* ENR indication. Though TLC can also engage in operando separations, it lacks the qualification of the required limit of detection (LOD, *e.g.* up to ~3900 μg/L in the dairy) (Choma et al., 2004). Although super high sensitivity could be reached by combining rolling circle amplification (RCA) with TdT catalysis as the item dubbed TdT-RCA (Du et al., 2019), it demanded strictly timed protocols including the horseradish peroxidase-catalyzed spectrophotometry. As for the rest, too time-consuming would be their main disability to cope with the POCT scenes.

4. Conclusions

In summary, a paper-based contraption was invented by manipulating the elements of sandwich aptasensor in the microfluidic circuitry. To maximize the pattern readability on strips, two improvements were tailored: **(1)** A robust color-developing amplifier was contrived by rational diblock copolymerization of AuNPs into a nonaggregate constraint with the effort of TdT. The TAuC-sensitized LFB prevails over the traditional colloidal gold chromatographic assay in three orders of magnitude lower LOD and an average 5.2-fold signal increase. **(2)** A common smartphone was retrofitted into a ratiometric transducer with a professional image-processing App that converts and conveys quantitive information. These perks afforded a high-performance LFB, which permits rapid, precise and portable diagnostics of ENR at its POCT with excellent specificity and sensitivity. More importantly, the potent fusion across intelligent perception and DNA-structured nanomanufacturing would offers a digital access to leverage the capacity of disposable biochemical detectors in times of the "Internet of Things" and the "Internet Plus".

Declaration of competing interest

The authors declare that they have no known competing financial interests or personal relationships that could have appeared to influence the work reported in this paper.

CRediT authorship contribution statement

Run Tian: Conceptualization, Investigation, Writing - original draft. **Jinyu Ji:** Conceptualization, Investigation. **Yumei Du:** Methodology. **Xiaojun Bian:** Data curation, Investigation. **Fulin Zhu:** Methodology. **Gang Liu:** Investigation. **Shengyuan Deng:** Data curation, Investigation. **Ying Wan:** Writing - review & editing, Supervision. **Juan Yan:** Validation, Supervision.

Acknowledgements

This project was financially supported by the National Major Special Project for the Development of Transgenic Organisms (2018ZX08011-04B), the National Natural Science Foundation of China (Grant No. 21775102, 21874071, 21775072), Outstanding Youth Foundation of Jiangsu Province (BK20170093), National Key Research and Development Program of China for International Science & Innovation Cooperation Major Project between Governments (2018YFE0113200).

Appendix A. Supplementary data

Supplementary data to this article can be found online at https://doi.org/10.1016/j.bios.2020.112218.

References

Ahmad Raston, N.H., Nguyen, V.T., Gu, M.B., 2017. Biosens. Bioelectron. 93, 21–25.
Amendola, V., Pilot, R., Frasconi, M., Maragò, O.M., Iatì, M.A., 2017. J Phys. Condens. 29, 203002.
Annan-Prah, A., Agbemafle, E., Asare, P.T., Akorli, S.Y., 2012. J. Vet. Adv. 2, 199–208.
Atencia, J., Beebe, D.J., 2005. Nature 437, 648–655.
Belmouaddine, H., Shi, M., Sanche, L., Houde, D., 2018. Phys. Chem. Chem. Phys. 20, 23403–23413.
Billah, M.M., Rana, S.M.M., Hossain, M.S., Saifuddin, A.K.M., Islam, S.K.M.A., Naim, Z., Barua, S., 2014. J. Antibiot. 67, 745–748.
Bishop, J.D., Hsieh, H.V., Gasperino, D.J., Weigl, B.H., 2019. Lab Chip 19, 2486–2499.
Blasco, C., Pico, Y., Andreu, V., 2009. Electrophoresis 30, 1698–1707.
Bostan, H.B., Danesh, N.M., Karimi, G., Ramezani, M., Shaegh, S.A.M., Youssefi, K., Charbgoo, F., Abnous, K., Taghdisi, S.M., 2017. Biosens. Bioelectron. 98, 168–179.
Boughougal, A., Cherchali, F.Z., Messai, A., Attik, N., Decoret, D., Hologne, M., Sanglar, C., Pilet, G., Tommasino, J.B., Luneau, D., 2018. New J. Chem. 42, 15346–15352.
Che, Y., Zinchenko, A., Murata, S., 2015. J. Colloid Interface Sci. 445, 364–370.
Chen, A., Yan, M., Yang, S., 2016a. Trends Anal. Chem. 80, 581–593.
Chen, A., Yang, S., 2015. Biosens. Bioelectron. 71, 230–242.
Chen, Y., Chen, Q., Han, M., Liu, J., Zhao, P., He, L., Zhang, Y., Niu, Y., Yang, W., Zhang, L., 2016b. Biosens. Bioelectron. 79, 430–434.
Choi, S., Hwang, J., Lee, S., Lim, D.W., Joo, H., Choo, J., 2017. Sensor. Actuator. B Chem. 240, 358–364.
Choma, I.M., Choma, A., Komaniecka, I., Pilorz, K., Staszczuk, K., 2004. J. Liq. Chromatogr. 27, 2071–2085.
Dalirirad, S., Steckl, A., 2018. Sensor. Actuator. B Chem. 283, 79–86.
Denadai, M., Cass, Q.B., 2015. J. Chromatogr. A 1418, 177–184.
Deng, S., Yan, J., Wang, F., Su, Y., Zhang, X., Li, Q., Liu, G., Fan, C., Pei, H., Wan, Y., 2019. Biosens. Bioelectron. 137, 263–270.
Ding, Y., Jiang, Z., Saha, K., Kim, C.S., Kim, S.T., Landis, R.F., Rotello, V.M., 2014. Mol. Ther. 22, 1075–1083.
Du, Y., Zhou, Y., Wen, Y., Bian, X., Xie, Y., Zhang, W., Liu, G., Yan, J., 2019. Mikrochim. Acta 186, 840.
Fowler, J.D., Suo, Z., 2006. Chem. Rev. 106, 2092–2110.
Free, A.H., Adams, E.C., Kercher, M.L., Free, H.M., Cook, M.H., 1957. Clin. Chem. 3, 163–168.
Fu, X., Cheng, Z., Yu, J., Choo, P., Chen, L., Choo, J., 2016. Biosens. Bioelectron. 78, 530–537.
Fu, X., Wen, J., Li, J., Lin, H., Liu, Y., Zhuang, X., Tian, C., Chen, L., 2019. Nanoscale 11, 15530–15536.
Gnoth, C., Johnson, S., 2014. Geburtshilfe Frauenheilkd 74, 661–669.
Grabar, K.C., Freeman, R.G., Hommer, M.B., Natan, M.J., 1995. Anal. Chem. 67, 735–743.
He, H., Liu, B., Wen, S., Liao, J., Lin, G., Zhou, J., Jin, D., 2018. Anal. Chem. 90, 12356–12360.
Hu, S., Fang, B., Huang, Z., Chen, Y., Liu, D., Xing, K., Peng, J., Lai, W., 2019. J. Dairy Sci. 102, 6037–6046.
Hurst, S.J., Lytton-Jean, A.K., Mirkin, C.A., 2006. Anal. Chem. 78, 8313–8318.
Janecko, N., Pokludova, L., Blahova, J., Svobodova, Z., Literak, I., 2016. Environ. Toxicol. Chem. 35, 2647–2656.
Jauset-Rubio, M., Svobodova, M., Mairal, T., McNeil, C., Keegan, N., El-Shahawi, M.S., Bashammakh, A.S., Alyoubi, A.O., O'Sullivan, C.K., 2016. Anal. Chem. 88, 10701–10709.
Kang, J.H., Asami, Y., Murata, M., Kitazaki, H., Sadanaga, N., Tokunaga, E., Shiotani, S., Okada, S., Maehara, Y., Niidome, T., Hashizume, M., 2010. Biosens. Bioelectron. 25, 1869–1874.
Kasetsirikul, S., Shiddiky, M.J.A., Nguyen, N., 2020. Microfluid. Nanofluidics 24, 17.
Kim, J.Y., Lee, J.S., 2009. Nano Lett. 9, 4564–4569.
Kim, N.G., Kim, M.A., Park, Y.I., Jung, T.S., Son, S.W., So, B., Kang, H.G., 2015. J. Vet. Sci. 16, 431–437.
Koczula, K.M., Gallotta, A., 2016. Essays Biochem. 60, 111–120.
Lee, S.H., Hwang, J., Kim, K., Jeon, J., Lee, S., Lee, J.K., Kang, M., Chung, D.R., Choo, J., 2019. Anal. Chem. 91, 12275–12282.
Li, S., Zhang, Y., Wen, W., Sheng, W., Wang, J., Wang, S., Wang, J., 2019. Biosens. Bioelectron. 133, 223–229.
Li, X., Ballerini, D.R., Shen, W., 2012. Biomicrofluidics 6, 11301–11313.
Li, Y.X., Zhang, X.L., Li, W., Lu, X.F., Liu, B., Wang, J., 2013. Environ. Monit. Assess. 185, 2211–2220.
Lin, B., Guan, Z., Song, Y., Song, E., Lu, Z., Liu, D., An, Y., Zhu, Z., Zhou, L., Yang, C., 2018. Lab Chip 18, 965–970.
Liu, X., Ren, J., Su, L., Gao, X., Tang, Y., Ma, T., Zhu, L., Li, J., 2017. Biosens. Bioelectron. 87, 203–208.
Lombardo-Agui, M., Garcia-Campana, A.M., Gamiz-Gracia, L., Blanco, C.C., 2010. J. Chromatogr. A 1217, 2237–2242.
Majdinasab, M., Mitsubayashi, K., Marty, J.L., 2019. Trends Biotechnol. 37, 898–915.
Preechakasedkit, P., Siangproh, W., Khongchareonporn, N., Ngamrojanavanich, N., Chailapakul, O., 2018. Biosens. Bioelectron. 102, 27–32.
Qi, J., Li, B., Zhou, N., Wang, X., Deng, D., Luo, L., Chen, L., 2019. Biosens. Bioelectron. 142, 111533–111536.
Quesada-González, D., Merkoçi, A., 2015 Biosens. Bioelectron 73, 47–63.
Quesada-Gonzalez, D., Sena-Torralba, A., Wicaksono, W.P., de la Escosura-Muniz, A., Ivandini, T.A., Merkoci, A., 2019. Biosens. Bioelectron. 132, 132–135.
Quesada-Gonzáleza, D., Stefanib, C., Gonzálezc, I., Escosura-Muñiza, A.l., Domingob, N., Mutjéc, P., Merkoçia, A., 2019. Biosens. Bioelectron. 141, 111407–111408.
Sato, K., Hosokawa, K., Maeda, M., 2003. J. Am. Chem. Soc. 125, 8102–8103.
Southern, E.M., 1979. Anal. Biochem. 100, 319–323.
Tayeb-Cherif, K., Peris-Vicente, J., Carda-Broch, S., Esteve-Romero, J., 2016. Food Chem. 202, 316–323.
Terrado-Campos, D., Tayeb-Cherif, K., Peris-Vicente, J., Carda-Broch, S., Esteve-Romero, J., 2017. Food Chem. 221, 1277–1284.
Tian, H., Wang, J., Zhang, Y., Li, S., Jiang, J., Tao, D., Zheng, N., 2016. J. Chromatogr. B 1033–1034, 172–179.
Trouchon, T., Lefebvre, S., 2016. Open J. Vet. Med. 6, 40–58.
Ung, T., Liz-Marzan, L.M., Mulvaney, P., 2002. Colloids Surf. A Physicochem. Eng. Asp. 202, 119–126.
Wan, Y., Wang, P., Su, Y., Wang, L., Pan, D., Aldalbahi, A., Yang, S., Zuo, X., 2015. ACS Appl. Mater. Interfaces 7, 25618–25623.
Wang, P., Wan, Y., Ali, A., Deng, S., Su, Y., Fan, C., Yang, S., 2016. Sci. China Chem. 59, 237–242.
Wang, R., Kim, K., Choi, N., Wang, X., Lee, J., Jeon, J.H., Rhie, G.-e., Choo, J., 2018. Sensor. Actuator. B Chem. 270, 72–79.
Wang, X., Choi, N., Cheng, Z., Ko, J., Chen, L., Choo, J., 2017. Anal. Chem. 89, 1163–1169.
Wu, C., Cho, T.J., Xu, J., Lee, D., Yang, B., Zachariah, M.R., 2010. Phys. Rev. E 81, 011406.
Xie, Q.Y., Wu, Y.H., Xiong, Q.R., Xu, H.Y., Xiong, Y.H., Liu, K., Jin, Y., Lai, W.H., 2014. Biosens. Bioelectron. 54, 262–265.
Xu, J., Li, X., Li, C., Chen, J., Xiao, Y.X., 2018. Food Chem. 242, 122–130.
Xu, X., Liu, L., Jia, Z., Shu, Y., 2015. Food Chem. 176, 219–225.
Zanchet, D., Micheel, C.M., Parak, W.J., Gerion, D., Williams, S.C., Alivisatos, A.P., 2002. J. Phys. Chem. B 106, 11758–11763.
Zhang, X., Gouriye, T., Göeken, K., Servos, M.R., Gill, R., Liu, J., 2013. J. Phys. Chem. C 117, 15677–15684.
Zhao, Y., Zhang, G., Liu, Q., Teng, M., Yang, J., Wang, J., 2008. J. Agric. Food Chem. 56, 12138–12142.
Zhou, W., Gao, X., Liu, D., Chen, X., 2015. Chem. Rev. 115, 10575–10636.